A Cost-Effective Approach for Achieving Subwavelength THz Imaging Using Photoinduced Coded-Apertures on Mesa-Array Structures

Yijing Deng , Student Member, IEEE, Yu Shi , Peizhao Li , Student Member, IEEE, Patrick Fay , Fellow, IEEE, Li-Jing Cheng, Member, IEEE, and Lei Liu , Senior Member, IEEE

Abstract-A novel and cost-effective approach for highresolution terahertz (THz) imaging using photoinduced (PI) codedapertures on micromachined mesa-array structures is reported. The mesa-array structures are designed to have subwavelength electrically isolated mesas for generation of high-fidelity photopatterns for THz imaging. An Si mesa-array prototype structure was successfully fabricated and tested. Measurements show that a modulation depth of \sim 22 dB was obtained in the frequency range of 740–750 GHz under a light intensity of 11.7 W/cm², which agrees well with theoretical analysis and full-wave simulation. Initial imaging experiments were first performed using 64 pixels (over different areas) for validation and performance evaluation. More advanced imaging using quadrupled pixel number (256 pixels) was conducted in order to resolve subwavelength features. As a result, a wavelength-scale spatial resolution of 400 μ m has been successfully demonstrated, and a subwavelength resolution as small as \sim 250 μ m (0.625 λ at 740 GHz) has been shown to be potentially achievable. The proposed PI coded-aperture imaging using mesa arrays is promising for developing real-time high-resolution THz imaging with simple system and low cost.

Index Terms—Coded-aperture imaging (CAI), mesa-array structure, photoinduced (PI) coded-apertures, terahertz (THz) imaging.

I. INTRODUCTION

HE terahertz (THz) frequency range (0.1–10 THz) sandwiched by microwaves and infrared light has remained the least explored and developed in the entire electromagnetic spectrum. However, in recent decades, unprecedented progress

Manuscript received 19 April 2022; revised 27 July 2022 and 24 August 2022; accepted 4 September 2022. Date of publication 26 September 2022; date of current version 7 November 2022. This work was supported in part by the National Science Foundation under Grant ECCS-1711631 and Grant ECCS-1711052, in part by the Center for Advanced Diagnostics and Therapeutics, and in part by the Center for Nanoscience and Technology at the University of Notre Dame, Notre Dame, IN, USA. This paper was presented at the IEEE/MTT-S IMS2021, Atlanta, GA, USA, June 6–11. (Corresponding author: Yijing Deng.)

Yijing Deng, Yu Shi, Peizhao Li, Patrick Fay, and Lei Liu are with the Electrical Engineering Department, University of Notre Dame, Notre Dame, IN 46556 USA (e-mail: ydeng2@nd.edu; yshi5@nd.edu; pli8@nd.edu; pfay@nd.edu; lliu3@nd.edu).

Li-Jing Cheng is with the School of Electrical Engineering and Computer Science, Oregon State University, Corvallis, OR 97331 USA (e-mail: chengli@eecs.oregonstate.edu).

This article has supplementary material provided by the authors and color versions of one or more figures available at https://doi.org/10.1109/TTHZ.2022.3209535.

Digital Object Identifier 10.1109/TTHZ.2022.3209535

has been achieved in THz applications owing to the major advances of THz signal generation and detection techniques. THz imaging has been extensively explored in a variety of fields from quality assurance to medical sensing [1], [2], [3], [4], [5], and subwavelength spatial resolution is especially important for many of those applications (e.g., for detection of small defects in materials [6], [7] and high-precision investigation of abnormal tissues [8], [9]). One conventional imaging approach is to use array sensors (e.g., focal plane arrays) [10], [11], [12], which requires large number of detectors (each detector incorporates a separate antenna module and additional read-out circuit), leading to increased system complexity and cost, as well as a small number of pixels hence limited spatial resolution. Nearfield scanning probe microscopy [13], [14], [15] is commonly employed to enable subwavelength THz imaging by focusing the incident radiation on a metallic tip that interacts with the imaging object in close proximity. However, it requires raster mechanical scanning of the subwavelength tip, resulting in a low imaging speed.

Those problems could be solved by using the coded-aperture imaging (CAI) technique [16], [17], [18]. CAI has attracted increasing attention in recent years owing to its capability of achieving system simplicity, high signal-to-noise ratio (SNR), high resolution, and potentially high image acquisition speed [19], [20]. In conventional THz CAI systems, Schottky diodes [21] or graphene modulators [22] are often employed to form coded-aperture masks for wavefront spatial modulation. However, the abovementioned mask implementation approaches require on-chip patterning and complex routing of biasing and control lines, which again leads to a small number of pixels as well as limited spatial resolution.

An alternative solution is to use optically generated free carriers in semiconductors [23] to form coded-aperture masks without the need for any prepatterned circuits/devices. Photoinduced CAI (PI-CAI) experiments have been performed using unpatterned Si substrates [24], [25], [26]; however, the achievable resolution (e.g., \sim 840 μ m in Si) was limited by the relatively large carrier diffusion length L_D (e.g., \sim 420 μ m in Si) [23]. To improve the achievable spatial resolution, imaging using ultrashort THz pulses (generated by a femtosecond laser pump) was performed by measuring the responses immediately after photoexcitations to minimize the impact of carrier lateral

2156-342X © 2022 IEEE. Personal use is permitted, but republication/redistribution requires IEEE permission. See https://www.ieee.org/publications/rights/index.html for more information.

diffusion in unpatterned Si [27]. Such system has a rigorous requirement for time resolution (in femtosecond scale), which is realized by splitting the incident laser pulse into two beams (for THz signal generation and detection, respectively [28]) and adding an additional delay line in one of the beam paths to control the path length difference with micrometer precision. Such requirement significantly increases the system complexity and cost. THz CAI based on the light-matter effect that is capable of exceeding the diffusion-length-determined resolution limit without using bulky laser modules and additional delay line is therefore highly desired. In view of this demand, we propose and demonstrate a novel approach for achieving subwavelength THz imaging using mesa-array-based PI-CAI. The mesa arrays facilitate the formation of high-fidelity photopatterns by confining optically induced free carriers inside each mesa [29]. Therefore, much smaller coded aperture pixels can be directly generated on the structure without the need of bulky femtosecond lasers and additional delay stage for low-cost subwavelength imaging. In addition, the mesa-array structure could be further implemented as a technology platform for realizing more advanced THz components, such as tunable and reconfigurable mesh filters [30].

In this article, we extend our earlier article in [31] and demonstrate a wavelength-scale THz CAI system using photopatterned mesa arrays. This is the first time that such high resolution has been demonstrated on long-carrier-lifetime semiconductors using constant optical light output and continuous THz waves. A prototype Si mesa-array structure was designed, fabricated, and fully characterized. Initial imaging experiments (64 pixels) were performed at 740 GHz ($\lambda = 405 \mu m$) for performance validation and evaluation. More advanced PI-CAI with 256 pixels shows that an imaging resolution of 0.625λ has been obtained; and letter-shaped objects have been imaged for wavelength-scale resolution validation. This level of resolution is not achievable if using unpatterned Si as the aperture mask [26]. Last but not least, key considerations affecting the performance of the proposed imaging approach are also discussed. The mesa-array-based PI-CAI is promising for developing cost-effective high-resolution real-time imaging and sensing systems.

II. PHOTOINDUCED CODED APERTURE IMAGING

By directly changing illuminated photopatterns and light intensities, coded-aperture masks can be virtually formed and optically reconfigured on photosensitive semiconducting materials (such as Si or Ge) [25]. Fig. 1 shows the schematic of a PI-CAI system. A digital mirror device (DMD) chipset is employed to redirect optical light from the source onto the semiconductor. The photopatterned semiconductor is placed in the THz beam path to simulate the function of wavefront encoding masks. By recording THz intensity (Y) at the detector, and with the knowledge of the mask matrix Ψ , a two-dimensional (2-D) profile ($X = \Psi^{-1}Y$) of electromagnetic field at the object plane can be reconstructed [32]. An orthogonal Hadamard matrix basis [33] is employed to generate PI-CAI masks for high-resolution imaging [34], [35].

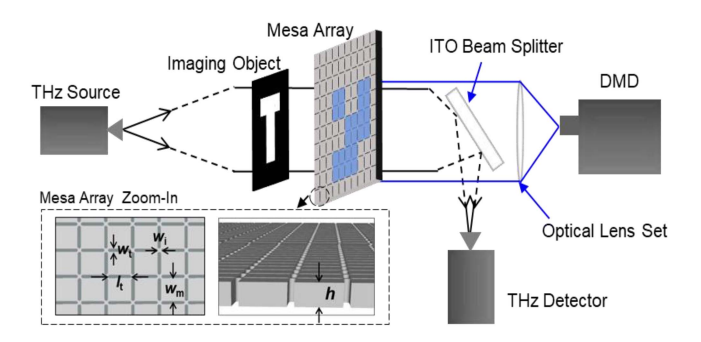


Fig. 1. Schematic of PI-CAI using optically patterned mesa arrays. Insets show zoomed-in figures of mesa arrays from top view and side view.

Based on this approach, PI-CAI has been implemented using unpatterned semiconductor as the aperture mask [26]. However, as discussed in Section I, the lateral diffusion of free carriers [23], [36] expands the pixel size and degrades the spatial resolution. To exceed the diffusion-length-determined limitation and improve spatial resolution to potentially subwavelength level, in this article, we propose to replace the unpatterned semiconductor substrate with micromachined mesa arrays. As can be seen from the inset of Fig. 1, the structure consists of a 2-D array of subwavelength mesas (mesa unit size: $w_m \times w_m$) separated by periodic vertical trenches (extending across the substrate; the trenches have lateral dimensions of $l_t \times w_t$). The adjacent mesas (electrically isolated by the trenches) are connected by small corner junctions $(w_i \times w_i)$ to prevent significant THz wave "leakage" through the trenches (more in-depth discussion is given in Section III). In addition, by using mesa-array structures, PI-free carriers can be effectively confined inside each subwavelength mesa (e.g., $w_m = 5 \mu \text{m}$, or $\sim \lambda/80$ at 740 GHz) without diffusing to unilluminated ones [36] (based on the carrier localization effect reported in other micromachined structures, such as quantum dots [37], [38] and nanowires [39]). As a result, high-fidelity photopatterns (or CAI pixels) with a resolution as small as w_m can be directly generated for subwavelength imaging (without the need for expensive THz TDS setup to generate ultrashort laser pulses). This resolution is far finer than the diffusion length L_D (e.g., \sim 420 μ m for Si, comparable to the $\lambda = 405 \ \mu m$ at 740 GHz), and is determined by the PI pixel size (fundamentally limited by the mesa unit size). The proposed PI-CAI approach utilizing micromachined electrically isolated mesa arrays eliminates the need of bulky laser module and additional delay line setup (to meet the rigorous time resolution requirement in THz TDS systems [28]). As a result, it provides a simple and cost-effective method for realizing high-resolution CAI.

III. MESA ARRAY DESIGN AND SIMULATION

To verify the validity of the proposed PI-CAI approach using mesa arrays, the optical modulation properties were first investigated through full-wave HFSS simulations. A 50 μ m thick, 20000- Ω ·cm high-resistivity silicon (HRS) substrate was used. The effective carrier lifetime of the HRS was assumed to be 30 μ s. A physics-based model [36], [40], [41] was employed

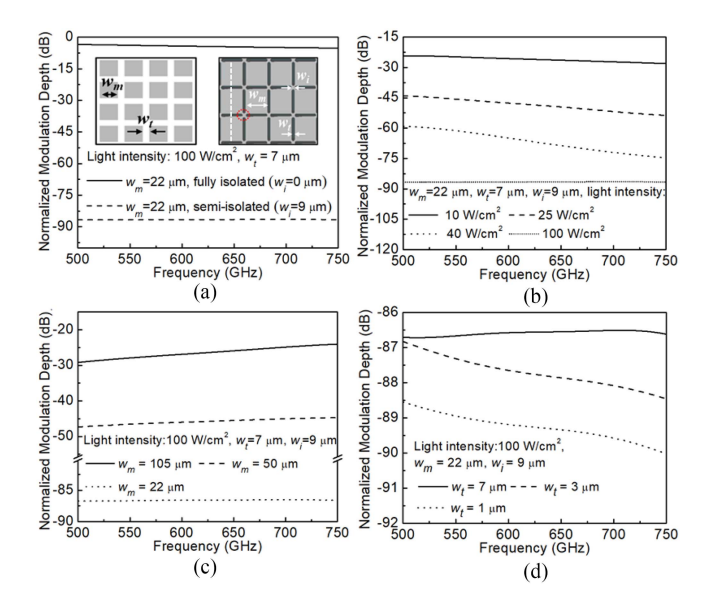


Fig. 2. Impact of (a) corner junctions, (b) light intensities, (c) mesa sizes, and (d) trench widths on the modulation depth. Insets in (a) show zoom-in illustrations of mesa array with fully isolated mesas and semi-isolated mesas (or with corner junctions).

for calculation of photogenerated free carrier concentration as well as photoconductivity. Two Floquet ports were assigned (in HFSS) to a single mesa unit cell to provide a plane wave excitation (normal to the mesa top surface) and mimic an infinite periodic array of mesas. Material parameters (e.g., conductivity) extracted from the physics-based model were assigned in HFSS to simulate the HRS under different light intensities. A normalized THz modulation depth (the transmission difference between the light "ON" and "OFF" states) was used for evaluation of the THz modulation mechanism.

An exemplary mesa array ($w_m = 22 \mu \text{m}$, $w_t = 7 \mu \text{m}$) with completely isolated mesas [without corner junctions, or $w_i =$ $0 \mu m$, see Fig. 2(a) left inset] was first investigated. It can be seen from Fig. 2(a) that only \sim 4 dB modulation depth (solid line) was obtained for this structure even under a strong light intensity of 100 W/cm². This is due to significant THz signal leakage through the trenches (much longer than the wavelength). By adding small corner junctions 9 μ m × 9 μ m [see red circle in Fig. 2(a) right inset] between adjacent mesas while keeping all the other design parameters the same, the modulation depth was increased to \sim 87 dB (dashed line). The introduction of the corner junctions ensures that the largest trench dimensions were much smaller than the THz wavelength. As a result, evanescent waves are generated near the mesa-array surface, and wave propagation through the gaps can be sufficiently suppressed for a higher modulation depth. In the following experiments, the design of mesa-array structures with corner junctions was utilized.

In addition to the impact of the corner junctions, light intensity also plays an important role in influencing the THz spatial modulation. Fig. 2(b) shows the simulation results for modified mesa array structure ($w_m = 22 \mu m$, $w_i = 9 \mu m$, and $w_t = 7 \mu m$) under different incident light intensities. It can be seen that the modulation depth has a positive correlation with the

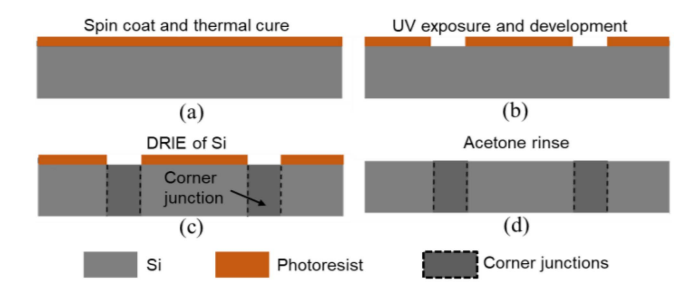


Fig. 3. Fabrication process flow for mesa arrays. (a) Spin coating photoresist on top surface of Si and thermal cure. (b) Contact lithography and development. (c) DRIE of Si from the top surface. (d) Photoresist removal.

light intensity, which is attributed to a larger photoconductivity and thus a higher THz absorption coefficient [42], [43] under elevated light intensities. In addition, the optical modulation depth of the mesa array can be further increased by decreasing the mesa size and the trench width [see Fig. 2(c) and (d)]. This is again due to reduced trench dimensions, and consequently higher suppression of THz "leakage" through the mesa array structure.

IV. MESA ARRAY FABRICATION AND MODULATION DEPTH CHARACTERIZATION

An Si mesa array structure was designed and fabricated for performance evaluation and initial experimental demonstrations. Based on previous theoretical analysis, the prototype mesa array was designed to have a mesa unit size $(w_m \times w_m)$ of $105~\mu\mathrm{m}~\times~105~\mu\mathrm{m}~(\sim\!0.26\lambda~\mathrm{at}~740~\mathrm{GHz})$ and trench lateral dimensions $(l_t \times w_t)$ of 96 μ m \times 7 μ m. The thickness of the Si substrate was chosen to be 50 μ m to maintain a trench aspect ratio (trench depth/trench width) of \sim 7 (50 μ m/7 μ m) for ease of fabrication [44]. The resistivity of the Si substrate was 20000-Ω·cm. Fig. 3 shows the fabrication process flow from a cross-section view of the Si structure [along a line parallel to the trenches, as indicated by the white dotted line in the right inset of Fig. 2(a)]. S1813 photoresist was first spin-coated on the wafer at 4000 rpm for 30 s to form a 1.4 μ m thin film, and was cured at 115°C for 60 s to remove most of the solvent, as shown in Fig. 3(a). The fabrication was followed by contact photolithography (for 4 s under a UV light intensity of 20 mW/cm²) and development (using AZ 917 MIF for 30 s) to form a sacrificial photomask on the top surface of the Si [Fig. 3(b)]. As shown in Fig. 3(c), deep reactive ion etching (DRIE) was then performed to form vertical trenches [45] on the Si substrate while maintaining corner junction structures (indicated in the dark grey areas). A combination of SF₆/C₄F₈ gases (for etching/passivation) was utilized in DRIE with a flux rate of 300/130 sccms and a circle time of 7/2 s. An average etching rate of \sim 5 μ m/min was obtained. The Si mesa array was cleaned with acetone to remove residual photoresist as shown in Fig. 3(d).

Fig. 4 shows the scanning electron microscopy images for the fabricated mesa array. It can be seen from Fig. 4(b) that the subwavelength-sized trenches have been successfully

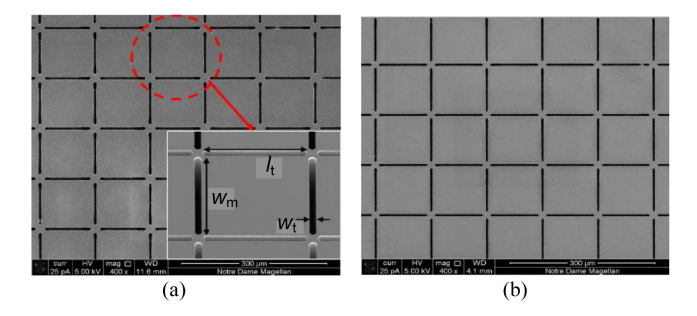


Fig. 4. Scanning electron microscopy (SEM) images of the fabricated mesa array from (a) top and (b) bottom surfaces. The inset in (a) gives a zoomed-in image of a single mesa unit.

etched through the Si substrate. However, note that due to microloading effect [46], the trench widths on the bottom surface were slightly narrower than those on the top. Furthermore, as shown in the high-magnification inset of Fig. 4(a), the corner junction structures were fabricated to meet our design expectations. The introduction of corner junctions not only facilitates higher modulation depth, but also maintains a structure that is sufficiently robust to be handled without the need for an additional supporting substrate beneath the mesas.

To validate the optical modulation mechanism, the fabricated Si mesa array was tested using an Agilent N5245A vector network analyzer (VNA) with two VDI WR-1.5 extenders to measure the transmission through the mesa array (under different light intensities). A set of optical lenses with short focal lengths was positioned between light source and the mesa array, allowing imaging area as well as light intensity to be controlled by adjusting the magnification. The highest light intensity achieved using current light source available in our lab was 11.7 W/cm² (this light intensity was also used in the following imaging experiments). The mesa array was placed at a distance of \sim 8 mm from the source to ensure that the corresponding THz beam diameter (~4.5 mm) was smaller than the optical illumination area (\sim 6 mm \times 6 mm) for effective THz modulation. To extract the optical modulation depths from all the other path losses (such as water absorption, Si insertion loss, etc.), the detected S_{21} were normalized to the S_{21} at light "OFF" state (0 W/cm²). Fig. 5 shows the modulation depths over the entire WR-1.5 frequency band (500–750 GHz). It can be seen that an average modulation depth of ~ 20 dB was obtained under a light intensity of ~ 11.7 W/cm², which agrees well with the theoretical analysis (in Section III) where a 30 μ s carrier lifetime was assumed for the HRS. Note that some ripples were observed in the measured modulation depth (dashed lines) due to standing wave resonances between VNA ports and the mesa array. Our simulations (Section III) have predicted that by engineering the mesa-array structure (for smaller trench sizes) and increasing the light intensity (e.g., to 100 W/cm²), a higher modulation depth could be achieved (~87 dB, see the gray solid line in Fig. 5). The proposed mesa-array-based approach with high modulation depth shows significant potential for realizing high-performance THz CAI.

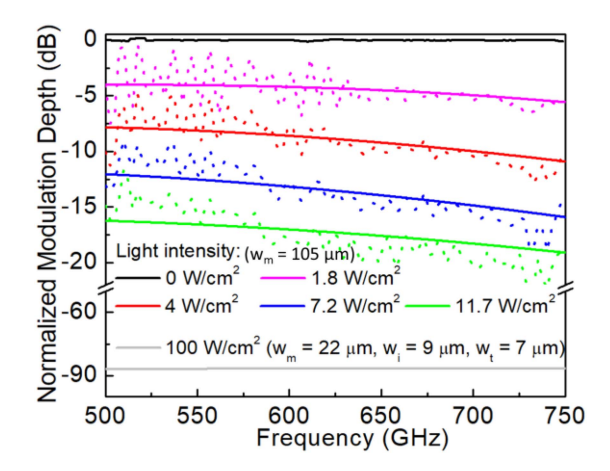


Fig. 5. Modulation depth of mesa array ($w_m = 105 \, \mu \text{m}$) in the frequency range of 500–750 GHz under different light intensities. Simulation results: solid lines, measured data: dashed lines. Simulation results for mesa array with smaller mesa unit size ($w_m = 22 \, \mu \text{m}$) and higher light intensity (100 W/cm²) were also provided (gray solid line) to show the potential.

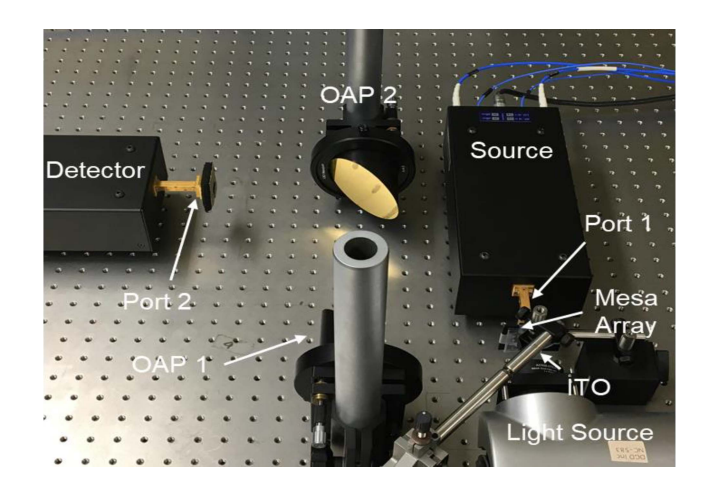


Fig. 6. Experiment setup for PI-CAI at 740 GHz using mesa array.

V. PI-CAI IMAGING RESULTS

To verify the PI-CAI approach using mesa arrays, several sets of experiments with increasing pixel numbers and decreasing imaging areas have been performed to explore and demonstrate the imaging capabilities (especially the achievable imaging resolution) step-by-step. The PI-CAI experiments were performed at 740 GHz using the fabricated mesa arrays. This frequency is just below the highest frequency in the WR-1.5 band (750 GHz, available using our current VNA setup with VDI extensions) and was chosen to avoid the strong water absorption peak near 750 GHz. The experimental setup is shown in Fig. 6 (corresponds to the schematic in Fig. 1). An indium tin oxide (ITO) substrate that has a high optical transmittance and a high THz conductivity was employed in the setup as a beam splitter to enable optical and THz beam paths to be merged simultaneously. The optical patterns originated from a programmable DMD chip were focused by a set of optical lenses, transmitted through the ITO substrate, and imaged on the mesa array for generation of coded apertures. Two WR-1.5 diagonal horn antennas were connected

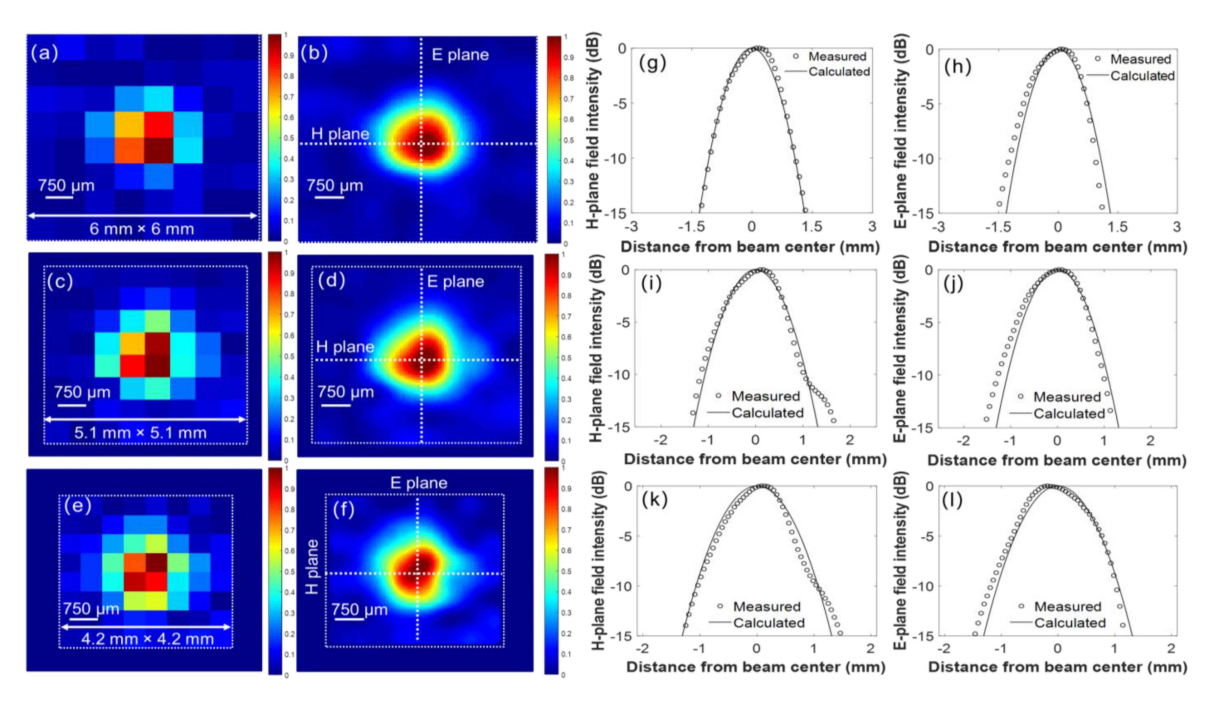


Fig. 7. (a), (c), and (e) Two-dimensional (2-D) imaging for THz radiation pattern. The imaging area was reduced from (a) 6 mm \times 6 mm to (c) 5.1 mm \times 5.1 mm, and (e) 4.2 mm \times 4.2 mm, and pixel number remains 8 \times 8 pixels. (b), (d), and (f) show median filtered images for better observation of the field distribution. (g), (i), and (k) Normalized 1-D field distribution extracted from radiation pattern in (b), (d), and (f) along H plane. Similarly, (h), (j), and (l) quantify the 1-D field distribution for radiation pattern in (b), (d), and (f) along E plane. The corresponding H planes and E planes were indicated in (b), (d), and (f) using white dotted lines. The measured 1-D field intensities were compared with the calculated Gaussian beam distributions, and show near Gaussian field distributions.

to VDI extenders at port 1 and port 2 of an Agilent N5245A VNA for THz signal generation and detection. The incident THz beam from the source was first transmitted through the object to be imaged, modulated by the optically patterned mesa array, and reflected off the ITO substrate. The THz beam was then collimated and focused by two off-axis parabolic mirrors and recorded at the detector. A MATLAB program was utilized to control the VNA and light source for automatic measurement and simultaneously process data for image reconstruction. We note that while VNA was employed here to provide THz signal generation and detection for initial experimental exploration, a much simpler and less expensive THz direct detector (such as Schottky diode detector [47]) can be utilized for a compact and lower cost system (compared to THz–TDS using bulky femtosecond lasers and additional delay stages) in principle.

A. Initial Validation of PI-CAI Using Mesa Arrays

To verify the validity of the proposed mesa-array-based PI-CAI approach, at 740 GHz, the field distribution of the THz radiation from port 1 (see Fig. 6) was examined using the mesa array. The THz radiation wavefront was modulated at a distance of \sim 3 mm from the source antenna. Based on Gaussian beam transformation [48], the beam diameter at this distance was calculated to be \sim 2.5 mm. Fig. 7(a)–(f) shows 2-D CAI results (8 \times 8 pixels) of the THz radiation for different areas. This 64-pixel-based imaging was first performed using a 6 mm \times 6 mm imaging area. The width of the square imaging area was then decreased to 5.1 and 4.2 mm (a reduction of 15% and 30%), respectively, while keeping the same number of pixels. The PI pixel size was reduced accordingly. As can be seen from the

reconstructed images, despite the decreasing imaging area, the beam diameter remains ~ 2.5 mm, which is consistent with the calculated result. In addition, by decreasing PI pixel size, more details of the field distribution can be observed [see Fig. 7(a), (c), and (e)]. Median filtered images [Fig. 7(b), (d), and (f)] were presented for better observation of the radiation pattern. Furthermore, the field distributions of the THz radiation were then quantified through normalized 1-D field intensities along H planes and E planes [see Fig. 7(b), (d), and (f)]. Theoretical Gaussian beam distributions were also calculated [48] for comparison. It can be seen from Fig. 7(g)–(1) that the measured 1-D field intensities (circles) agree well with the calculated results (solid lines), which verify the proposed PI-CAI using mesa array is working as expected.

B. Further Investigation of Imaging Capabilities

In addition to the initial validation, PI-CAI experiments were performed at 740 GHz to image a set of parallel slots separated by a distance of 800 μm . Fig. 8(a) shows the slots object (linewidth of 800 μm and length of 3 mm) being imaged. To accommodate the slots dimensions, imaging was performed by placing the object at a distance of $\sim\!\!16$ mm from the source antenna (see port 1 in Fig. 6) to obtain a THz beam diameter of $\sim\!\!5$ mm (larger than the slot dimension). Fig. 8(b) shows the 8 \times 8 pixels imaging result without the slots over a 6 mm \times 6 mm area (each pixel has a dimension of 750 $\mu m \times 750~\mu m$). It can be seen that by increasing the distance between the object and the antenna, larger THz beam size was achieved as expected (compared to that in Fig. 7, where a beam diameter of $\sim\!\!2.5$ mm was obtained for a distance of 3 mm). The slots object was then placed within the

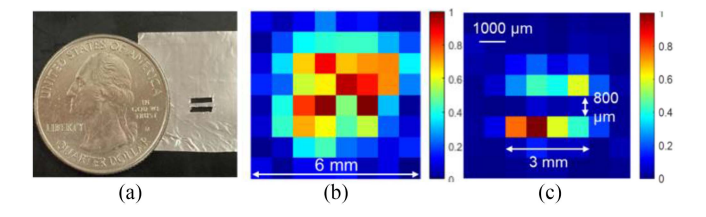


Fig. 8. 8 × 8 pixels imaging for parallel slots (800 μ m wide and 3 mm long). The distance between those slots is ~800 μ m. (a) Optical image of the slots object placed next to a U.S. quarter. (b) 8 × 8 pixels imaging of the THz beam without slots object. The imaging was performed at ~16 mm away from the antenna (port 1) to obtain a THz beam diameter of ~5 mm (exceeds the largest dimension of the object). (c) 8 × 8 pixels THz CAI imaging with parallel slots. The imaging area was 6 mm × 6 mm for both (b) and (c).

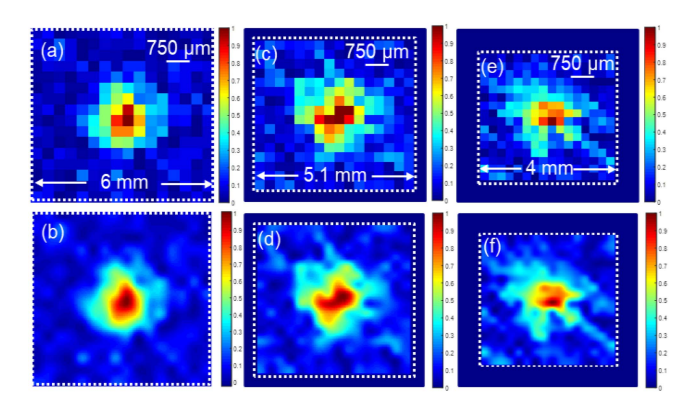


Fig. 9. Zooming-in imaging of a THz beam for subwavelength feature observation. The direct mapping of THz beam was performed at 740 GHz from a distance of 3 mm from the antenna. (a), (c), and (e) 16×16 pixels with imaging area decreased from 6 mm \times 6 mm to 5.1 mm \times 5.1 mm, and 4 mm \times 4 mm. (b), (d), and (f) Corresponding median filtered images.

near-field region (\sim 50 μ m) of the mesa array to take advantage of the evanescent fields [49]. The imaging result in Fig. 8(c) shows a one-pixel wide (750 μ m) gap between two parallel lines, which is consistent with the distance between the slots, reflecting a resolution of better than 800 μ m has been achieved.

C. Demonstration of Field Distribution in Subwavelength Scale

To resolve subwavelength features, the PI pixel number was quadrupled from 8×8 pixels to 16×16 pixels to achieve subwavelength-scale pixel sizes. Three different imaging areas, $6.0 \text{ mm} \times 6.0 \text{ mm}$, $5.1 \text{ mm} \times 5.1 \text{ mm}$, and $4.0 \text{ mm} \times 4.0 \text{ mm}$, were used as shown in Fig. 10. By reducing the imaging area (from $6.0 \text{ mm} \times 6.0 \text{ mm}$ to $4.0 \text{ mm} \times 4.0 \text{ mm}$), the PI pixel sizes were decreased from $375 \text{ to } 250 \,\mu\text{m}$ (or from 0.91λ to 0.625λ at 740 GHz). The THz beam was directly modulated by the mesa array at a distance of 3 mm away from the horn antenna (port 1 in Fig. 6). The corresponding THz beam diameter is $\sim 2.5 \text{ mm}$. As can be seen from Fig. 9(a)–(f), by decreasing the imaging area, the image of the THz beam was magnified, and more details of the field distribution can be revealed in a subwavelength scale. The smallest pixel size in this demonstration [i.e., Fig. 9(e)] was nearly $250 \,\mu\text{m}$, indicating that a system imaging resolution

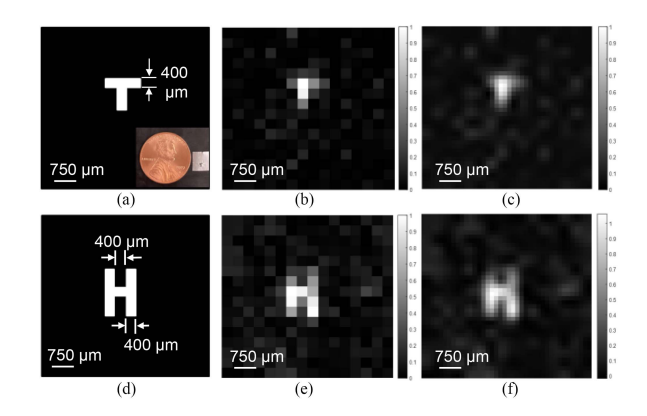


Fig. 10. Initial imaging results for stencils with wavelength-scale features [cut on Al foil ($16 \mu m$ thick)]. (a), (d) Illustration of T- and H-shaped imaging objects. The inset in Fig. 10(a) shows the comparison of the T-shaped stencil and a U.S. penny. (b), (e) 16×16 pixels imaging results for the imaging objects. (c), (f) show the corresponding median-filtered image for better observation of the object. The imaging areas were kept to be 6 mm \times 6 mm.

of \sim 250 μ m (0.625 λ) has been achieved. Using the fabricated Si mesa array in this article, and by using refined alignment, an imaging resolution as high as 105 μ m (determined by the mesa unit size) could potentially be achieved. However, we note that, by using a decreased pixel size (e.g., 250 μ m, which is only \sim 2.5 times of the mesa unit size) for PI-CAI, the effect of misalignment between PI pixels and mesas on the imaging quality may become more significant, and more artifacts can be observed in the resulting images. This could be solved by decreasing the mesa size (e.g., to 5 μ m) to be much smaller than the PI pixel size (more in-depth discussion will be elaborated in Section VI). Moreover, for larger pixel numbers (e.g., 16 × 16 pixels in this experiment), the transmission fluctuations during the initial imaging experiments have larger impact on the image reconstruction process. To reduce the impact of signal drift and ambient environment changes on the imaging quality, renormalization was performed by taking the intensity difference of detected signals before and after every Hadamard mask projection.

D. Resolution Validation Using Imaging Objects With Wavelength-Scale Features

The proposed high-resolution THz PI-CAI using mesa array can be applied for imaging of objects with wavelength-scale features. For initial demonstration, a set of letter-shaped stencils ["T" and "H" as shown in Fig. 10(a) and (d)] were used as the imaging objects. The linewidths were \sim 400 μ m for both objects, and the height was 1.5 mm for letter "T" and 2 mm for letter "H." By placing the object at a distance of \sim 16 mm from the horn antenna (the source), a large THz beam (\sim 5 mm in diameter) can be obtained at the imaging plane to accommodate the object dimension. The mesa array was placed closely to the object for near-field imaging. Fig. 10(b) shows the initial imaging result for the T-shaped aperture in gray colormap, and the critical features of the letter "T" are correctly presented at the middle part of the image. Imaging result for the more complex letter-H object is shown in Fig. 10(e), and the gap between

the two vertical slots was discerned, showing that an imaging resolution of better than \sim 400 μ m has been demonstrated. This result once again validated the observation of \sim 250 μ m system resolution indicated in the previous experiment in Section V part C [see Fig. 9(e)]. For clearer observation of the objects, median filtering was performed, and the resulting images are shown in Fig. 10(c) and (f). This level of resolution is well below the diffusion-length-determined pixel size possible with unpatterned Si. In addition, the demonstrated resolution is smaller than the free space wavelength of 405 μ m at 740 GHz. In principle, an imaging resolution approaching the mesa unit size (105 μ m) should be able to be demonstrated using the current mesa arrays. More refined high-quality images can be achieved by using more pixels, better pixel-mesa alignment, and higher light intensity (for higher THz modulation depth). The proposed PI-CAI using mesa array are promising in many other applications, such as high-precision boundary assessment for abnormal tissues.

VI. PI-CAI PERFORMANCE EVALUATION AND DISCUSSION

On the basis of previous imaging results, the performance of mesa-array-based PI-CAI was evaluated and discussed, including the spatial resolution, modulation-depth-related SNR and image contrast, as well as imaging speed.

A. Imaging Resolution

One of the key considerations for the proposed mesa-array-based PI-CAI is the spatial imaging resolution. Since optical illumination that is continuous in the time domain were employed (compared to ultrashort light pulses in [27]), a larger penetration depth of the photogenerated free carriers $h_{\rm opt}$ can be achieved in the mesa-array substrate ($h_{\rm opt}=h$, if $h < L_D$). As a result, high spatial frequency information (provided by the subwavelength-pixel modulating masks) can be effectively transmitted to the imaging objects (placed in the near field to the mesa array). Therefore, the minimum resolvable feature dimension is no longer limited by the diffraction of the THz beam on the modulation plane, but rather is primarily affected by the PI pixel size (which is eventually determined by the mesa unit size).

Since photogenerated free carriers are confined inside each isolated mesa (and cannot diffuse to adjacent ones), the achievable resolution using mesa array will be integer multiples of single mesa unit size (w_m) . However, in implementation, it is necessary to consider the misalignment between the PI pixels and the mesas themselves. In fact, due to the misalignment, the imaging resolution could be degraded by at least w_m , resulting in an actual pixel size of $w_p + w_m$ (w_p is the PI pixel size). The effect of such misalignment is especially significant when w_p is comparable to w_m , in which case more artifacts would be observed in the reconstructed images (see Section VI-C). This impact of misalignment could be minimized by using a w_m (e.g., 5 μ m) that is much smaller than w_p . Another solution is to use more sophisticated optical system (incorporates a microscope assembly [50]) to ensure precise alignment between the PI pixels and the mesas. The mesa arrays are capable of realizing subwavelength imaging (also exceeding the diffusion-length limit), and could be implemented as a platform for enabling more

advanced optically tunable/reconfigurable components [30] at even higher THz frequencies.

B. Effect of Modulation Depth on SNR and Image Quality

Other important factors in PI-CAI performance evaluation are the SNR and image quality that are significantly affected by the achievable THz modulation depth using the mesa array. In this article, the optically generated coded-aperture masks consist of PI pixels and intrinsic pixels ("opaque" or "transparent" to the transmitted THz radiations, corresponding to the "0"s and "1" s in the complementary Hadamard matrices [25]). However, in implementation, the PI pixels are not ideally "opaque" (due to limited photoconductivity or signal "leakage" through trenches), and THz radiation transmitted through these nominally "OFF" pixels is recorded at the detector, degrading the SNR. To achieve high image quality, it is therefore of importance to obtain a high modulation depth at the PI pixels.

The proposed mesa-array structure is capable of providing high modulation depth from two different aspects. First, by confining free carriers inside each mesa (with proper passivation [51] and/or annealing [52] process to reduce surface trap densities), a higher carrier concentration (or photoconductivity) can be obtained for higher modulation depth, comparing to that achievable using unpattern semiconductors (lateral diffusion of free carriers lowers the carrier concentration) [36]. By using semiconductors with higher carrier lifetime τ (e.g., Ge, with a typical $\tau = 1000 \,\mu\text{s}$) [40], the carrier concentration can be further increased for a higher modulation depth (without degrading achievable spatial resolution due to the usage of mesa array, but can potentially cause a slower image acquisition speed). Second, the mesa arrays are designed to have corner junctions as well as small trench dimensions for higher suppression of the THz wave "leakage." As discussed in Section III, a modulation depth of 87 dB could be realized by employing the modified mesa array with corner junctions ($w_t = 7 \mu \text{m}$, $w_m = 22 \mu \text{m}$, under a light intensity of 100 W/cm²), and a much improved SNR and PI-CAI imaging quality can be achieved.

C. Image Acquisition Speed

The speed to obtain a single frame image is important for enabling real-time THz imaging applications. There are two main aspects that impact the imaging speed for the proposed mesa-array-based PI-CAI. One is the switching speed of DMD chipset. For prototype demonstrations of PI-CAI experiments, the current DMD provides a frame rate of 1.3 kHz. However, this is not a fundamental limitation; the frame rate can be greatly improved by employing higher speed DMD chipsets (e.g., Texas Instrument DLPC410) for potential demonstration of real-time imaging. Another more important factor is the carrier lifetime of photogenerated free carriers. The Si mesa array employed for initial PI-CAI experiments has a carrier lifetime of $\tau = 30 \,\mu s$ (see discussion in Section III), which provides a 3-dB modulation bandwidth of \sim 6.7 kHz (\sim 1/(5 τ)). The carrier lifetime can be reduced by using HRS with a lower resistivity (or higher doping level). Specifically, by employing a mesa array with a shorter carrier lifetime of 1 μs , a bandwidth of 200 kHz could be obtained. However, it is worth pointing out that the

modulation depth will be simultaneously decreased if using smaller carrier lifetimes. Moreover, computational techniques, such as compressed sensing [53], can be employed in CAI to further increase the imaging speed.

VII. CONCLUSION

A novel approach of THz PI-CAI capable of resolving wavelength-scaled features has been demonstrated using mesa-array structures. An Si mesa array was designed, fabricated, and tested. Initial imaging experiments were performed at 740 GHz to verify the validity of the proposed approach and explore imaging capabilities, and a subwavelength imaging resolution (0.625λ) has been successfully demonstrated. Higher resolution could be achieved by using mesa arrays with smaller unit sizes. In addition, the mesa arrays offer a platform for realizing more advanced tunable/reconfigurable components at even higher THz frequencies. The proposed mesa-array-based PI-CAI approach is promising in developing more advanced high-resolution real-time THz imaging and sensing applications in a cost-effective manner.

ACKNOWLEDGMENT

The authors would like to thank the Advanced Diagnostics and Therapeutics Initiative and the Center for Nanoscience and Technology at the University of Notre Dame. The authors would also like to acknowledge the valuable assistance from the Virginia Diodes, Inc.

REFERENCES

- [1] G. OK, K. Park, H. J. Kim, H. S. Chun, and S.-W. Choi, "High-speed terahertz imaging toward food quality inspection," *Appl. Opt.*, vol. 53, no. 7, pp. 1406–1412, 2014.
- [2] D. Meledin et al., "A 1.3-THz balanced waveguide HEB mixer for the APEX telescope," *IEEE Trans. Microw. Theory Techn.*, vol. 57, no. 1, pp. 89–98, Jan. 2009.
- [3] A. W. M. Lee, B. S. Williams, S. Kumar, Q. Hu, and J. L. Reno, "Real-time imaging using a 4.3-THz quantum cascade laser and a 320×240 microbolometer focal-plane array," *IEEE Photon. Technol. Lett.*, vol. 18, no. 13, pp. 1415–1417, Jul. 2006.
- [4] H. Zhong, A. Sanchez, and X. Zhang, "Identification and classification of chemicals using terahertz reflective spectroscopic focal-plane imaging system," Opt. Exp., vol. 14, no. 20, pp. 9130–9141, 2006.
- [5] P. H. Siegel, "Terahertz technology in biology and medicine," *IEEE Trans. Microw. Theory Techn.*, vol. 56, no. 10, pp. 2438–2447, Oct. 2004.
- [6] H. Zhong et al., "Nondestructive defect identification with terahertz time-of-flight tomography," *IEEE Sensors J.*, vol. 5, no. 5, pp. 203–208, Apr. 2005.
- [7] D. Zimdars et al., "Technology and applications of terahertz imaging non-destructive examination: Inspection of space shuttle sprayed on foam insulation," in *Proc. 31st Annu. Rev. Prog. Quantitative Nondestruct. Eval.*, 2005, pp. 570–577.
- [8] T. C. Bowman, M. El-Shenawee, and L. K. Campbell, "Terahertz imaging of excised breast tumor tissue on paraffin sections," *IEEE Trans. Antennas Propag.*, vol. 63, no. 5, pp. 2088–2097, May 2015.
- [9] P. Tewari et al., "In vivo terahertz imaging of rat skin burns," *J. Biomed. Opt.*, vol. 17, no. 4, 2012, Art. no. 040503.
- [10] L. Liu, H. Xu, A. W. Lichtenberger, and R. M. Weikle, II, "Integrated 585 GHz hot-electron mixer focal-plane arrays based on annular-slot antennas for imaging applications," *IEEE Trans. Microw. Theory Techn.*, vol. 58, no. 7, pp. 1943–1951, Jul. 2010.
- [11] A. Lee and Q. Hu, "Real-time, continuous-wave terahertz imaging by use of a microbolometer focal-plane array," Opt. Lett., vol. 30, pp. 2563–2565, 2005

- [12] G. C. Trichopoulos, H. L. Mosbacker, D. Burdette, and K. Sertel, "A broadband focal plane array camera for real-time THz imaging applications," *IEEE Trans. Antennas Propag.*, vol. 61, no. 4, pp. 1733–1740, Apr. 2013.
- [13] N. C. J. V. D. Valk and P. C. M. Planken, "Electro-optic detection of subwavelength terahertz spot sizes in the near field of a metal tip," *Appl. Phys. Lett.*, vol. 81, pp. 1558–1560, 2002.
- [14] H. T. Chen, R. Kersting, and G. C. Cho, "Terahertz imaging with nanometer resolution," *Appl. Phys. Lett.*, vol. 83, pp. 3009–3011, 2003.
- [15] A. J. Huber, F. Keilmann, J. Wittborn, J. Aizpurua, and R. Hillenbrand, "Terahertz near-field nanoscopy of nanodevices," *Nano Lett.*, vol. 8, pp. 3766–3770, 2008.
- [16] W. L. Chan et al., "A single-pixel terahertz imaging system based on compressed sensing," Appl. Phys. Lett., vol. 93, no. 12, pp. 1–4, 2008.
- [17] H. Shen et al., "Spinning disk for compressive imaging," Opt. Lett., vol. 37, pp. 46–48, 2012.
- [18] Y. C. Shen et al., "Terahertz pulsed spectroscopic imaging using optimized binary masks," Appl. Phys. Lett., vol. 95, 2009, Art. no. 231112.
- [19] Z. Zhang, X. Ma, and J. Zhong, "Single-pixel imaging by means of Fourier spectrum acquisition," *Nature Commun.*, vol. 6, 2015, Art. no. 6225.
- [20] R. I. Stantchev, X. Yu, T. Blu, and E. Pickwell-MacPherson, "Real-time terahertz imaging with a single-pixel detector," *Nature Commun.*, vol. 11, 2020, Art. no. 2535.
- [21] S. Hawasli, N. Alijabarri, and R. M. Weikle II, "Schottky diode arrays for submillimeter-wave sideband generation," in *Proc. Int. Conf. Infrared, Millimeter, THz Waves*, 2012, pp. 1–2.
- [22] B. Sensale-Rodriguez et al., "Terahertz imaging employing graphene modulator arrays," *Opt. Exp.*, vol. 21, no. 2, pp. 2324–2330, 2013.
- [23] N. W. Ashcroft and N. D. Mermin, Solid State Physics. Washington, DC, USA: Saunders College Publishing, 1976.
- [24] L.-J. Cheng and L. Liu, "Optical modulation of continuous terahertz waves towards cost-effective reconfigurable quasi-optical terahertz components," *Opt. Exp.*, vol. 21, no. 23, pp. 28657–28667, 2013.
- [25] A. Kannegulla et al., "Coded-aperture imaging using photo-induced reconfigurable aperture arrays for mapping terahertz beams," *IEEE Trans. Terahertz Sci. Technol.*, vol. 4, no. 3, pp. 321–327, May 2014.
- [26] M. I. B. Shams et al., "A 740-GHz dynamic two-dimensional beamsteering and forming antenna based on photo-induced reconfigurable fresnel zone plates," *IEEE Trans. Terahertz Sci. Technol.*, vol. 7, no. 3, pp. 310–319, May 2017.
- [27] R. I. Stantchev et al., "Noninvasive, near-field terahertz imaging of hidden objects using a single-pixel detector," Sci. Adv., vol. 2, 2016, Art. no. e1600190.
- [28] C. A. S. Jens Neu, "Tutorial: An introduction to terahertz time domain spectroscopy (THz-TDS)," J. Appl. Phys., vol. 124, 2018, Art. no. 231101.
- [29] Y. Deng et al., "Advanced photo-induced substrate-integrated waveguides using pillar-array structures for tunable and reconfigurable THz circuits," *Opt. Exp.*, vol. 28, pp. 7259–7273, 2020.
- [30] Y. Deng, Y. Shi, P. Fay, and L. Liu, "Computational analysis of optically controlled reconfigurable terahertz mesh filters using mesa arrays," *Mi*crow. Opt. Technol. Lett., vol. 63, no. 7, pp. 1972–1977, 2021.
- [31] Y. Deng, Y. Shi, P. Li, P. Fay, and L. Liu, "Photo-induced coded-aperture imaging at 740 GHz using mesa arrays for achieving subwavelength resolution," in *Proc. IEEE/MTT-S Int. Microw. Symp.*, 2021, pp. 717–720.
- [32] W. Cheney and D. Kincaid, *Numerical Mathematics and Computing*, 6th ed. Pacific Grove, CA, USA: Thompson Brooks/Cole, 2008.
- [33] M. Harwit and N. J. Sloane, Hadamard Transform Optics. San Diego, CA, USA: Academic Press, 1979.
- [34] D. Shrekenhamer, C. M. Watts, and W. J. Padilla, "Terahertz single pixel imaging with an optically controlled dynamic spatial light modulator," *Opt. Exp.*, vol. 21, no. 10, pp. 12507–12518, 2013.
- [35] I. Valova and Y. Kosugi, "Hadamard-based image decomposition and compression," *IEEE Trans. Inf. Technol. Biomed.*, vol. 4, no. 4, pp. 306–319, Dec. 2000.
- [36] A. Kannegulla, M. Shams, L. Liu, and L.-J. Cheng, "Photo-induced spatial modulation of THz waves: Opportunities and limitations," *Opt. Exp.*, vol. 23, pp. 32098–32112, 2015.
- [37] M. Maximov et al., "Light emitting devices based on quantum well-dots," Appl. Sci., vol. 10, 2020, Art. no. 1038.
- [38] J. K. Kim, R. L. Naone, and L. A. Coldren, "Lateral carrier confinement in miniature lasers using quantum dots," *IEEE J. Sel. Top. Quantum Electron.*, vol. 6, no. 3, pp. 504–510, May/Jun. 2000.
- [39] M. G. Michelle et al., "Direct imaging of free carrier and trap carrier motion in silicon nanowires by spatially-separated femtosecond pump—probe microscopy," *Nano Lett.*, vol. 13, no. 3, pp. 1336–1340, 2013.

- [40] N. Joshi, Photoconductivity: Art: Science & Technology, 1st ed. Evanston, IL, USA: Routledge, 1990.
- [41] Y. Zhou and S. Lucyszyn, "Modelling of reconfigurable terahertz integrated architecture (RETINA) SIW structures," *Prog. Electromagn. Res.*, vol. 105, pp. 71–92, 2010.
- [42] H. Alius and G. Dodel, "Amplitude-, phase-, and frequency modulation of farinfrared radiation by optical excitation of silicon," *Infrared Phys.*, vol. 32, pp. 1–11, 1991.
- [43] Z. Jiang et al., "Investigation and demonstration of a WR-4.3 optically controlled waveguide attenuator," *IEEE Trans. Terahertz Sci. Technol.*, vol. 7, no. 1, pp. 20–26, Jan. 2017.
- [44] R. Abdolvand and F. Ayazi, "An advanced reactive ion etching process for very high aspect-ratio sub-micron wide trenches in silicon," *Sensors Act.* A Phys., vol. 144, no. 1, pp. 109–116, 2008.
- [45] K.-S. Chen, A. A. Ayon, X. Zhang, and S. M. Spearing, "Effect of process parameters on the surface morphology and mechanical performance of silicon structures after deep reactive ion etching (DRIE)," *J. Microelectro-mach. Syst.*, vol. 11, no. 3, pp. 264–275, 2002.
- [46] J. Yeom, Y. Wu, J. C. Selby, and M. A. Shannon, "Maximum achievable aspect ratio in deep reactive ion etching of silicon due to aspect ratio dependent transport and the microloading effect," *J. Vac. Sci. Technol. B*, vol. 23, no. 6, pp. 2319–2329, 2005.
- [47] "Virginia Diodes, Inc." [Online]. Available: http://vadiodes.com/index.php/en/
- [48] P. F. Goldsmith, Quasioptical Systems: Gaussian Beam Quasioptical Propagation and Applications. Piscataway, NJ, USA: Wiley-IEEE Press, 1998
- [49] J. Goodman, Introduction to Fourier Optics, 2nd ed. New York, NY, USA: McGraw-Hill, 1996.
- [50] DLi Digital Light Innovations. [Online]. Available: https://dlinnovations. com/
- [51] R. S. Bonilla, B. Hoex, P. Hamer, and P. R. Wilshaw, "Dielectric surface passivation for silicon solar cells: A review," *Phys. Status Solidi A*, vol. 214, no. 7, 2017, Art. no. 1700293.
- [52] N. S. Zin, A. Blakers, and K. Weber, "RIE-induced carrier lifetime degradation," *Prog. Photovolt.*, vol. 18, no. 3, pp. 214–220, 2010.
- [53] M. I. B. Shams et al., "Approaching real-time terahertz imaging with photo-induced coded apertures and compressed sensing," *Electron. Lett.*, vol. 50, no. 11, pp. 801–803, 2014.



Yijing Deng (Student Member, IEEE) is currently working toward the Ph.D. degree in electrical engineering with the University of Notre Dame, Notre Dame, IN, USA.



Yu Shi received the B.S. and M.S. degrees in optical engineering from the Huazhong University of Science and Technology, Wuhan, China, in 2010 and 2013, respectively. He is currently working toward the Ph.D. degree in electrical engineering with the University of Notre Dame, Notre Dame, IN, USA.



Peizhao Li (Student Member, IEEE) was born in Chengdu, China, in 1994. He received the B.S. degree in electronic information engineering from the Tianjin University of Technology, Tianjin, China, in 2017, and the M.S. degree in electrical engineering from the Washington State University, Vancouver, WA, USA, in 2020. He is currently working toward the Ph.D. degree in electrical engineering with the University of Notre Dame, Notre Dame, IN, USA.

His research interests include mm-wave to THz circuits and systems (e.g., phased arrays, RF switches, and reconfigurable filters).



Patrick Fay (Fellow, IEEE) received the Ph.D. degree in electrical engineering from the University of Illinois at Urbana–Champaign, Champaign, IL, USA, in 1996

He is currently a Professor with the Department of Electrical Engineering, University of Notre Dame, Notre Dame, IN, USA. He established the High Speed Circuits and Devices Laboratory, Notre Dame, and oversaw the design, construction, and commissioning of the 9000-ft2 class 100 cleanroom housed in Stinson-Remick Hall at Notre Dame. He has been

serving as the Director of this facility, since 2003. He has authored/coauthored 11 book chapters and more than 300 articles in scientific journals and conference proceedings. His research interests include design, fabrication, and characterization of microwave- and millimeter-wave electronic devices and circuits, the use of micromachining techniques for the fabrication of RF through submillimeter-wave packaging, and power devices.

Prof. Fay is a Distinguished Lecturer of the IEEE Electron Devices Society.



Li-Jing Cheng (Member, IEEE) received the B.S. and M.S. degrees in electronics engineering from the National Chiao Tung University, Hsinchu, Taiwan, in 1998 and 2000, respectively, and the Ph.D. degree in electrical engineering from the University of Michigan, Ann Arbor, MI, USA, in 2008.

He is currently an Associate Professor with the School of Electrical Engineering and Computer Science, Oregon State University, Corvallis, OR, USA. From 2010 to 2013, he was a Research Assistant Professor of chemical engineering with the University

of Notre Dame, Notre Dame, IN, USA. His research interests include materials and scalable nanofabrication for electronic, photonic, and THz devices, and lab-on-a-chip technologies for biomedical applications.



Lei Liu (Senior Member, IEEE) received the B.S. and M.S. degrees in electrical engineering from the Nanjing University, Nanjing, China, in 1998 and 2001, respectively, and the Ph.D. degree in electrical engineering from the University of Virginia, Charlottesville, VA, USA, in 2007.

From 2007 to 2009, he was a Postdoctoral Research Associate with the Department of Electrical and Computer Engineering, University of Virginia. In 2009, he joined the University of Notre Dame, Notre Dame, IN, USA, as a Faculty Member, where he is

currently an Associate Professor of electrical engineering. He has authored or coauthored more than 140 journal and conference papers. His research interests include millimeter- and submillimeter-wave device and circuit design, modeling, and testing, quasi-optical techniques, terahertz detectors for imaging and spectroscopy, novel microwave materials and devices, superconducting electronics, microfabrication, and processing.

Dr. Liu served as a Session Chair for the 2006 IEEE Applied Superconductivity Conference, a Session Co-Chair for the 2015, 2018, and 2022 IEEE International Microwave Symposium, and a Student Paper Competition Judge for the 2011 and 2017 IEEE MTT-S IMS. He is the recipient of the IEEE MTT-S THz Prize (IEEE Transactions on Terahertz Science and Technology Best Paper Award) in 2019. His students were the recipients of the 2012 IEEE Asia—Pacific Microwave Conference (Taiwan) Student Prize, the 2012 International Conference on Infrared, Millimeter and Terahertz Waves (Wollongong, Australia) Best Student Paper Award, the 2015 IEEE MTT-S Graduate Fellowship Award, and the 2019 MTT-S International Microwave Conference on 5G and Beyond Best Student Paper Award (first place).